

FEM Modeling of the Reinforcement Mechanism of Hydroxyapatite in PLLA Scaffolds, Produced by Supercritical Drying, to be used for Tissue Engineering Applications

L. Baldino^{1,†}, F. Naddeo^{2,†}, S. Cardea^{1,*}, A. Naddeo^{1,*}, E. Reverchon^{1,3}

¹ Department of Industrial Engineering, University of Salerno, Via Giovanni Paolo II, 132, 84084, Fisciano (SA), Italy

² Department of Information Engineering, Electrical Engineering and Applied Mathematics, University of Salerno, Via Giovanni Paolo II, 132, 84084, Fisciano (SA), Italy

³ NANO_MATES, Research Centre for Nanomaterials and Nanotechnology, University of Salerno, Via Giovanni Paolo II, 132, 84084, Fisciano (SA), Italy

[†] These authors equally contributed

* Corresponding authors information: scardea@unisa.it, +39 089969365; anaddeo@unisa.it, +39 089964061

Authors information:

Lucia Baldino lbaldino@unisa.it, +39 089964232
Francesco Naddeo fnaddeo@unisa.it, +39 089964061
Ernesto Reverchon ereverchon@unisa.it, +39 089964116

Abstract

Scaffolds have been produced by supercritical CO₂ drying of Poly-L-Lactid Acid (PLLA) gels loaded with micrometric fructose particles used as a porogen. These structures show a microporous architecture generated by voids left in the solid material by porogen leaching, maintaining in the meanwhile nanostructure of the original gel, formed by a network of nanofilaments. The scaffolds have also been loaded with hydroxyapatite (HA) nanoparticles, from 10 to 50 % w/w with respect to the polymer, in order to improve the mechanical properties of PLLA structure.

In this work, we propose a parametric Finite Element Method (FEM) model of the PLLA-HA composite that takes into account the microporous structure, modeled starting from the concept of the close-packing of equal spheres and the nanoscale structure, modeled as a regular space frame of

isotropic curved fibers. The effect of HA on the mechanical properties of the scaffolds has been modeled through the formation concentric cylinders of HA nanoparticles on PLLA nanofibers. This assumption has been developed on the basis of SEM images taken on the section of PLLA+HA scaffolds.

Modeling analysis confirms that mechanical properties of these scaffolds depend on nanofibrous network connections in the space and that bending is the major mode of deformation of the network. FEM model also contains the information of the fact that HA creates a multi-layer coating on some areas in the fiber network that tend to increase in thickness when HA percentage is increased. Young modulus trend, evaluated experimentally, tends to a plateau, for HA percentages larger than 30 % w/w, when the coverage of the nanofibers produced by HA nanoparticles reaches a loaded surface index of 0.14 in the FEM model. A further increase of HA percentage only slightly contributes to the mechanical properties of the scaffold. This last observation is confirmed in the FEM model and can be attributed to nanoparticles deposition on the bottom of micropores.

Keywords: Scaffold, Supercritical Fluids, Poly(l-lactic acid) nanofibers, Hydroxyapatite nanoparticles, FEM modeling.

1 Introduction

One of the crucial steps in Tissue Engineering (TE) is the scaffold fabrication. A scaffold is a 3-D construct which works as a temporary support for human cells, during the formation of the new tissue. A new generation of engineered tissues is based on the development of nanoporous degradable polymeric scaffolds containing additives such as ceramics (for example, hydroxyapatite), bioactive molecules (for example, growth factors) or drugs (anti-inflammatory agents or antibiotics) (Cardea et al., 2014; Malafaya et al., 2002a, b).

The first important parameter for loaded scaffolds fabrication is the selection of the materials. For example, scaffolding materials for bone TE should be osteoconductive to favor the adhesion and migration of the osteoprogenitor cells on the scaffolds, that subsequently, differentiate and form the new bone (Costantino and Friedman, 1994; Goldberg, 1992). Biodegradable polymers have been widely proposed to develop porous 3-D scaffolds (Ma and Zhang, 1999; Reverchon et al., 2012; Zhang and Ma, 1999a, b); among them, we can consider Poly(lactic acid) (PLA), Poly(glycolic acid) (PGA) and their copolymers (PLGA). These synthetic materials demonstrated to be biocompatible and to decompose in vivo into non-toxic components with a controllable degradation rate (Ma and Zhang, 1999). Another important class of materials for bone repair is represented by ceramic compounds, such as Hydroxyapatite (HA) (Flautre et al., 2001; Li et al., 2002; Visscher et al., 1985), which is similar to the mineral part of the natural bone and shows good osteoconductivity and bonding ability (LeGeros, 2002).

To combine the osteoconductivity of HA and the biodegradability of biopolymers, polymer/ceramic composite scaffolds have been proposed for bone TE (Reverchon and Adami, 2013; Zhang and Ma, 1999a, b), that can mimic the natural bone composition; indeed, natural bone is composed of inorganic (mainly HA, at the nanometric scale) and organic compounds (mainly Collagen) that form the extracellular matrix (ECM). A key characteristic in scaffolds fabrication is their “architecture”, that should mimic the one of natural bone, assuring adequate cell-environment interactions. In particular, some characteristics have to be simultaneously obtained, such as

microporosity, characterized by large interconnections between pores, and nanofibrous substructure, resembling the one of the natural ECM, to allow cells adhesion and migration on and inside the scaffold and to obtain proper mechanical properties (Zhang and Ma, 1999a, b).

Several techniques have been proposed for polymeric scaffolds fabrication, that include: fiber bonding, solvent casting, particulate leaching, melt molding, solid free form fabrication, gas foaming, freeze drying combined with particulate leaching and electrospinning. Details about these processes can be found in various reviews (Ma, 2004; Stamatialis et al., 2008). However, these techniques suffer of several limitations; particularly, it is very difficult to obtain simultaneously macro, micro and nanostructural characteristics and the proper mechanical properties that are required for the various TE applications.

Supercritical carbon dioxide (SC-CO₂) assisted processes have been proposed to overcome the limitations of traditional techniques in several fields (Baldino et al., 2014b; Cardea and Reverchon, 2011; Prosapio et al., 2014; Reverchon and Cardea, 2005; Reverchon et al., 1994; Reverchon et al., 2009; Subra et al., 1998) due to their processing flexibility and gas-like mass transfer properties. Some SC-CO₂ assisted processes have also been proposed for TE applications (Baldino et al., 2014a; Reverchon and Cardea, 2012): supercritical induced phase separation (SC-IPS) (Cardea et al., 2006; Duarte et al., 2009), supercritical foaming (Harris et al., 1998; Mooney et al., 1996), supercritical gel drying combined with particulate leaching (Pisanti et al., 2012; Reverchon et al., 2008; Reverchon et al., 2009) and electrospinning in SC-CO₂ (Levit and Tepper, 2004; Liu et al., 2010). The aims of SC-CO₂ assisted techniques applied to TE is to modulate mass transfer properties and to obtain an efficient solvent elimination, due to the large affinity of SC-CO₂ with almost all the organic solvents, and to work using short processing times (Brunner, 2010). A promising technique, from the point of view of the reproduction of the fibrous nanostructure of bones, is supercritical gel drying combined with particulate leaching. Indeed, the scaffolds produced using this process, show several advantages with respect to those obtained using the other techniques: controlled and large open porosity (> 90 %), large internal surface areas, very large

connectivity at micrometric level and preservation of the natural structure of nanofibrous polymeric aerogels. In particular, it is possible to assure the coexistence of the micro and nanostructural characteristics necessary for bone TE. Using this process, Reverchon et al. (Reverchon et al., 2009) prepared Poly(l-lactic acid) (PLLA)-HA composite scaffolds, adding nanometric HA particles in the starting solution, with the aim of optimizing the composition and the mechanical characteristics of the produced structures. Indeed, HA is one of the major components of natural bone and its addition increases the mechanical resistance of the structure. These scaffolds were successfully tested in static and dynamic cultivation of human Mesenchymal Stem Cells (hMSCs) (Pisanti et al., 2012); these results indicated that hMSCs were able to adhere, proliferate, differentiate into the scaffolds and calcium deposition started.

Considering the importance of the mechanical properties of scaffolds and the difficulties in developing a comprehensive interpretation of the experimental results, modeling and simulation can be a relevant support in the development of scaffolds with appropriate mechanical characteristics.

Computer-Aided Tissue Engineering (CATE) is generally based on a set of additive manufacturing techniques for the fabrication of patient-specific scaffolds, starting from geometries obtained from medical imaging. One of the major problems about the application of CATE is the definition of the internal architecture of the scaffolds (Rainer et al., 2012). In the scientific literature, some studies on non parametric computational models based on finite element method (FEM) and computational fluid dynamics, developed to analyze composite scaffolds in the context of bones regeneration, have been performed (Milan et al., 2009; Sandino et al., 2008). In most cases, a micro-computed tomography scan of the scaffold has been used (Hu et al., 2009) and the results showed that, when the cells were cultured in a bioreactor, their displacement was primarily determined by scaffold morphology (Jungreuthmayer et al., 2009) and the stress distribution induced by fluid perfusion was largely dependent on pores distribution within the scaffold (Olivares et al., 2009). Other papers are based on the optimization of scaffold microstructure using triply periodic minimal surfaces and forming processes based on rapid prototyping techniques (Kapfer et

al., 2011; Rajagopalan and Robb, 2006). However, modeling hypotheses are rarely supported by direct micro and nanometric information about the scaffold, derived from the experimentally produced structures.

Therefore, in the present work, mechanical characteristics of PLLA nanostructured scaffolds loaded with HA nanoparticles have been characterized with the support of Scanning Electron Microscope (SEM) images. Nanometric scaffolds modifications induced by HA loading have been evidenced. Based on these experimental information, a parametric FEM model has been proposed in this work.

2 Materials and Methods

2.1 Materials

PLLA L210 (M_w 210000) was purchased from Boehringer Ingelheim (Ingelheim, Germany), d-fructose (m.p. 119-122 °C), Dioxane, Ethanol (99.8 % purity) and Hydroxyapatite nanoparticles (particle size < 200 nm) were bought from Sigma Aldrich (S. Louis, MO, USA); CO₂ (99 % purity) was purchased from SON (Società Ossigeno Napoli - Italy). All materials were used as received.

2.2 Preparation of the composite scaffolds

Scaffolds were prepared according to the procedures reported in a previous work (Reverchon et al., 2009). Solutions at PLLA at concentration of 15 % w/w in Dioxane were prepared; then, Ethanol, as the non-solvent, was added, obtaining a Dioxane/Ethanol ratio of 1.7. The solution was stirred and heated at 60 °C until it became homogeneous. Then, fructose microparticles were added with a mean diameter of 250 μm, together with HA nanoparticles (diameter < 200 nm), forming a gel suspension. The gel was dried, to eliminate the two organic solvents, using SC-CO₂ at 200 bar, 35 °C for 4 hours (Reverchon et al., 2009); the obtained structures were rinsed in distilled water for 24 hours to eliminate all fructose particles. Then, the scaffolds were put in an oven for 12 hours at 40 °C, to evaporate water.

2.3 Characterizations

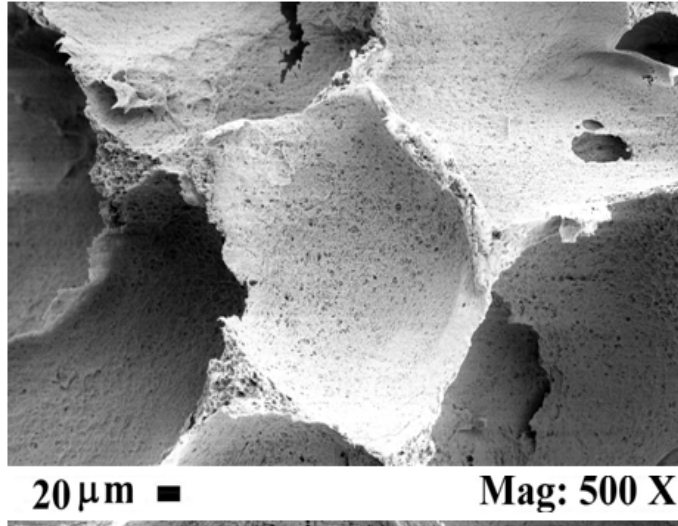
PLLA-HA scaffolds nanostructure was extensively analyzed by SEM (mod. LEO 1525, Carl Zeiss SMT AG, Oberkochen, Germany) and HA dispersion in the scaffolds was evidenced using an Energy Dispersive X-Ray analyzer (EDX) (mod. INCA Energy 350, Oxford Instruments, Witney, UK), using the signal of Calcium atoms to characterize HA nanoparticles.

The porosity of the scaffolds was calculated from the density of the scaffold and the density of untreated PLLA. The compressive mechanical properties of the scaffolds were measured using an INSTRON 4301 (Instron Int. Ltd, High Wycombe, UK): cylindrical samples with a diameter of 2 cm and a thickness of 4 mm were compressed at a cross-head speed of 1 mm/min.

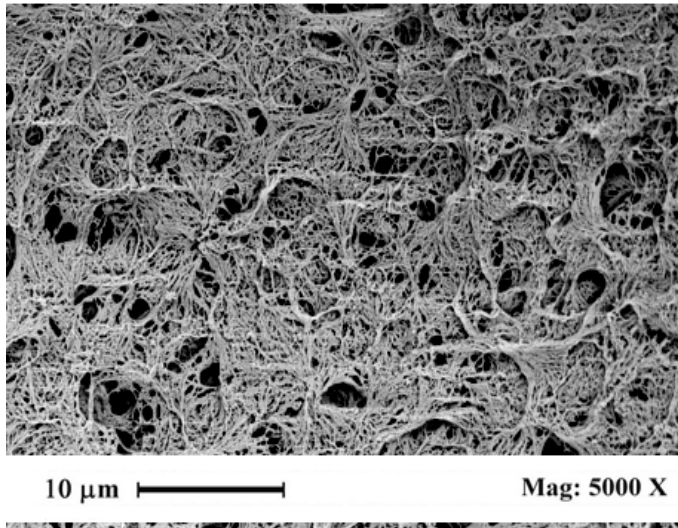
3 Experimental results

In the first part of the work, we reproduced and extended the supercritical gel drying results obtained in a previous work (Reverchon et al., 2009). In particular, we focused the attention on the influence of HA nanoparticles percentage loaded in PLLA on the nano and micro morphology and on the mechanical resistance of these scaffolds. HA percentages up to 50 % w/w were tested.

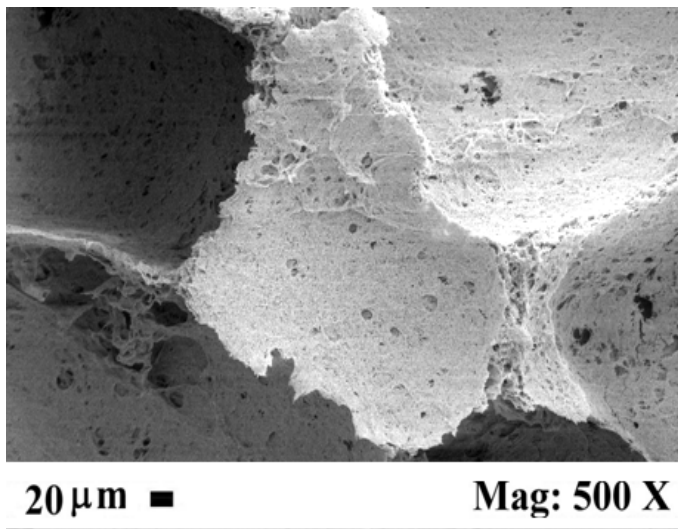
In Figure 1, SEM images of PLLA scaffolds generated as reported in the “Preparation of the composite scaffolds” paragraph, with different HA content (from 10 to 50 % w/w of PLLA) have been reported. It is evident that all of them are characterized by the presence of the microporous structure induced by the presence of porogen particles (Figures 1a, 1c) and by an uniform nanometric network related to the gel structure (Figures 1b, 1d). Part of HA nanoparticles tends to adhere on PLLA fibers, probably, as a result of electrostatic forces acting among nanoparticles and polymer (see Figure 2b and compare it with Figure 2a in which an unloaded PLLA scaffold is reported).



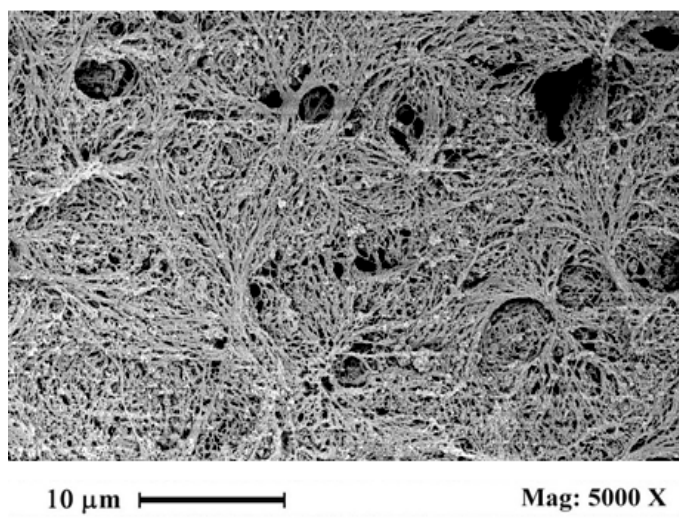
(a)



(b)



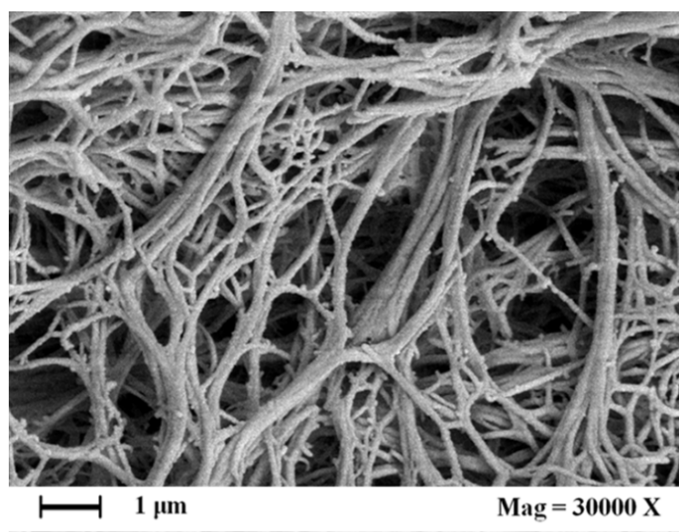
(c)



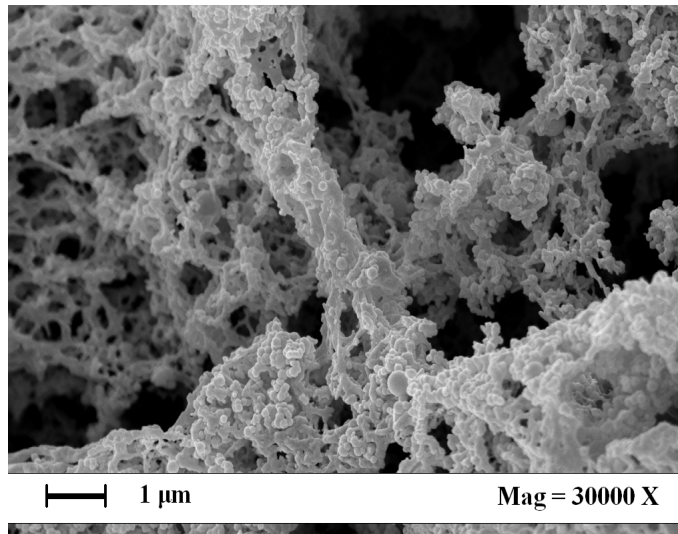
(d)

Figure 1: PLLA/HA scaffolds obtained by SC-CO₂ drying at 200 bar and 35 °C, with a-b) 10 % w/w HA, c-d) 50 % w/w HA.

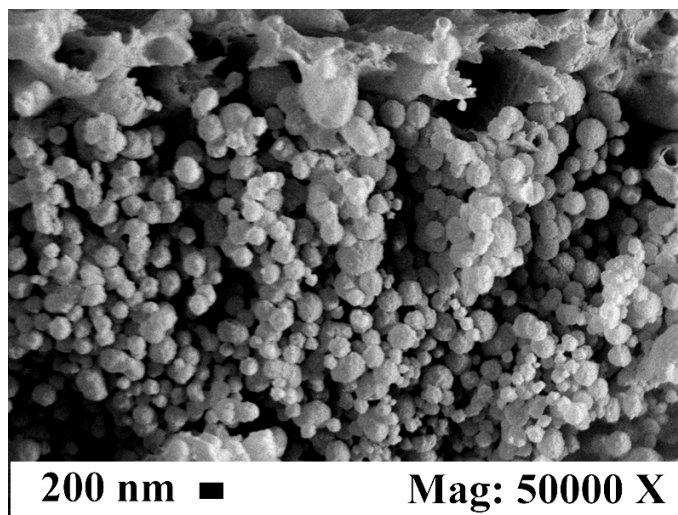
At high loadings, HA nanoparticles also tend to deposit on the bottom of the pores of the polymeric structure. These experimental evidences can be noticed from SEM image reported in Figure 2a in which PLLA nanofibers related to a scaffold not loaded with HA are shown; moreover, in Figure 2b, HA decorated nanofibers and HA decoration in multiple layers is clearly visible, whereas in Figure 2c, a SEM image of HA nanoparticles found on the bottom of a micropore is reported.



(a)



(b)



(c)

Figure 2: PLLA scaffolds obtained by SC-CO₂ drying at 200 bar and 35 °C, a) 15 % w/w PLLA, b) 15 % w/w PLLA + 50 % w/w HA, c) HA nanoparticles on the bottom of a PLLA micropore, 50 % w/w HA.

In the scaffolds with a HA content equal or lower than 30 % w/w, no accumulation of nanoparticles is evidenced on the bottom of micropores. It is also relevant that the presence of HA nanoparticles does not modify the microporous and the macroporous structure; i.e., dimension and shape of the pores and of the scaffolds.

Another possible problem is the possible agglomeration of HA nanoparticles in the scaffold. For this reason, we verified the overall HA nanoparticles distribution inside the scaffold structure using EDX. Figure 3 confirms that a relatively uniform distribution of HA has been obtained for a 30 % w/w loading.

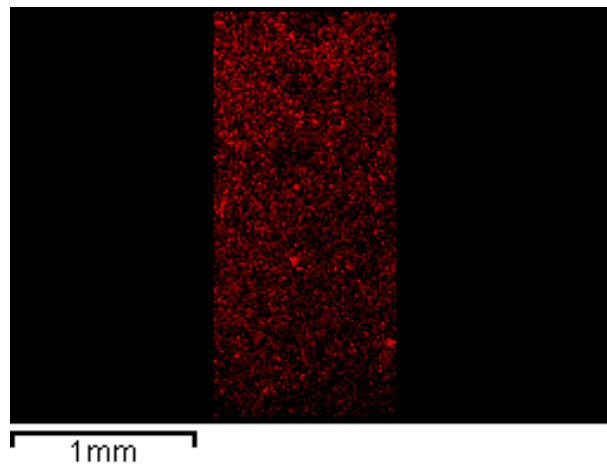


Figure 3: HA nanoparticles distribution (measured through the Calcium atoms distribution - red) along the section of a PLLA scaffold with 30 % w/w of HA.

Once verified the morphology of the scaffolds and the distribution of HA nanoparticles, we focused the attention on the mechanical characteristics of PLLA+HA scaffolds. We analyzed the compressive modulus of PLLA scaffolds starting from pure PLLA and using increasing percentages of HA nanoparticles. These results are reported in Table 1. The loading of HA nanoparticles inside the structure produces a large increase of the compressive modulus from 81 to 122 kPa, thus overcoming the compressive modulus that is usually set as the optimum for bone temporary scaffolds (100 kPa). These results are similar to those obtained in a previous work (Reverchon et al., 2009), confirming the good reproducibility of the process.

PLLA, % w/w	HA, % w/w PLLA	Compressive Modulus, kPa
15	0	81 ± 1.5
15	10	107 ± 1.8
15	30	120 ± 2.0
15	50	122 ± 2.5

Table 1: Compressive modulus of PLLA scaffolds obtained with different HA contents.

A first explanation of these results can be given considering that HA nanoparticles inside the nanofibrous structure of the scaffold reinforce the overall structure producing a higher mechanical resistance. However, as we will see in the modeling section, more intriguing scenarios are possible. In principle, it could be possible to find a compromise between the nanofibrous structure of non-loaded PLLA scaffolds, the fibrous+nanoparticle structure of PLLA+HA scaffolds and the obtained mechanical resistance. The better compromise seems to be represented by PLLA scaffolds containing 30 % w/w of HA, considering that the loading of 50 % w/w of HA nanoparticles produces a negligible increase of the compressive modulus (Table 1). Moreover, cultivation of hMSCs in the same PLLA+HA scaffolds loaded with 250 μ m porogen demonstrated that they were the most appropriate for hMSCs migration, proliferation and differentiation. Effects of the architecture of the scaffold were magnified in dynamic culture, leading to an increased proliferation and osteoblastic differentiation, evidenced by alkaline phosphates (ALP) and bone morphogenic protein-2 (BMP-2) expression (Pisanti et al., 2012).

4 FEM modeling and results

In this part of the work, we focused our attention on the realization of parametric FEM models, that can give a proper representation of the experimental evidences. PLLA scaffolds generated in this work are characterized by two kinds of porosity: at micrometric and at nanometric level. Therefore, FEM models must be able to:

- reproduce the nanometric and micrometric porosity;

- allow the realization of a sensitivity analysis, to find the parameters on which to focus the modeling and to verify the hypothesized mechanisms of reinforcement;
- successful reproduce experimental results.

The results obtained in this work are generated by the appropriate interaction of two FEM models as will be explained in details in the following paragraphs: a FEM model representing the microscale porosity and a FEM model representing the nanoscale porosity.

4.1 Modeling the micrometric porous structure

The porogen, as discussed in the experimental section, consists of fructose particles with a mean diameter of 250 μm , that can be modeled as spheres, with a good degree of approximation. It formed a suspension in the polymeric solution that was, then, compressed at 10 bar to produce a contact among porogen particles, inducing the interconnection among the pores of the final structure. In the hypothesis that the spherical particles have all the same diameters, it is possible to approximate the structure as a “Close-packing of equal spheres”; i.e., a dense arrangement of congruent spheres in an infinite, regular arrangement. The greatest fraction of space that can be occupied by spheres, in regular lattice arrangement, is 0.74.

There are two simple regular lattices that achieve this highest average density; they are called face-centered cubic (fcc) and hexagonal close-packed (hcp) (Figure 4). Both are based on sheets of spheres arranged at the vertices of a triangular tiling; they differ in how the sheets are stacked upon one another (Figure 4). The direction of compression coincides with the direction of the compression mechanical testing and is the same of the axis of the cylindrical container. This fact is in favor of the adoption of the hexagonal close-packed (hcp) modeling.

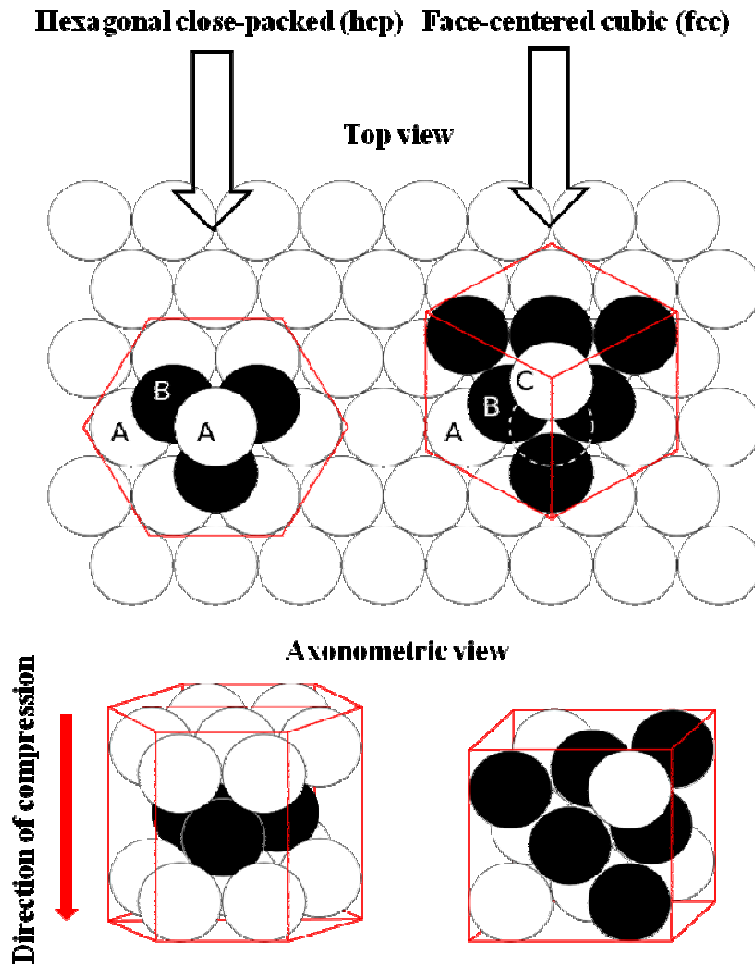


Figure 4: hcp (left) and fcc (right) close-packing of spheres.

4.1.1 Identification of the representative volume element (RVE)

In finite element modeling, the representative volume element (RVE) is the smallest volume element investigated; it is large enough to contain all the intrinsic characteristics of the real structure to be simulated (material properties and geometrical characteristics). We selected a porous hexagonal prism, based on the theory of hcp, according to which, there is a spherical pore arrangement of ABA type. The A layer is formed by 7 spherical pores; whereas, the B layer consists of 3 spherical pores (Figure 4 on the left). For this purpose, in the *Ansys* FEM simulation environment, we wrote an algorithm that, depending on the porosity, is able to realize the geometrical RVE model previously described, using a Newton-Raphson method to approximate the porosity (see Figure 5). The micrometric porosity was calculated on the basis of the specific weight

of the polymer, of the amount by weight of fructose particles and of the other components contained in the gel. It is equal to about 0.8. Remembering that, in hcp distribution, in condition of tangency among the spheres, the maximum accessible porosity is equal to about 0.74, the algorithm used to model the desired porosity (0.8) produces some intersections among the spheres. This fact results in the formation of holes that connect the pores of the structure, as in the experimental evidences.

In the second step, the algorithm realizes an identical mesh on the two bases of the prism; therefore, displacement boundary conditions on counterpart nodes to simulate the compression test can be applied.

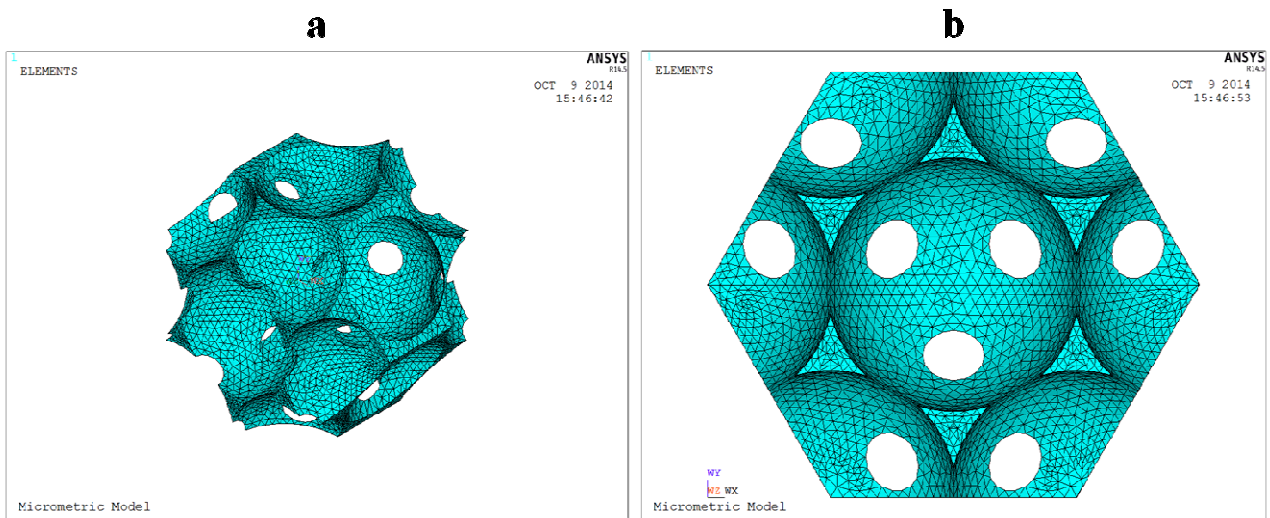


Figure 5: RVE FEM model (micrometric structure level): a) 3D view; b) Top view.

The use of an identical mesh, on opposite sides of the porous hexagonal prism, allows us to apply the following boundary conditions on the displacements related to homologous nodes lying on opposite sides:

$$\begin{cases} u_2 = \varepsilon_{xx}L + u_1 \\ v_2 = v_1 \\ w_2 = w_1 \end{cases} \quad (1)$$

being u , v and w the three displacement components of opposite nodes, indicated with 1 and 2 subscripts; ε_{xx} the imposed deformation along the x axis (prism axis); L the length.

The Cauchy Tensor associated to this test presents negligible components compared to σ_{xx} component; therefore, we can easily calculate the homogenized Young modulus, using the following relationship:

$$E_{xx} = \frac{\langle \sigma_{xxi} \rangle}{\langle \varepsilon_{xx} \rangle} \quad (2)$$

being $\langle \varepsilon_{xx} \rangle$ the strain component applied to the RVE in the x direction; and

$$\langle \sigma_{xxi} \rangle = \frac{\sum \sigma_{xxi} v_i}{V_p} \quad (3)$$

in which σ_{xxi} is the x normal component of the Cauchy Tensor and v_i the volume of the i -th finite element of the model; V_p the volume of the pore-free virtual hexagonal prismatic RVE. This algorithm can calculate $\langle \sigma_{xx} \rangle$ also as:

$$\langle \sigma_{xx} \rangle = \frac{\sum F_i}{A} \quad (4)$$

being F_i the x component of the reaction nodal force applied to the i -th node, lying on one of the basis of the prism, and A the surface of the hexagonal basis. These two different methods of calculation produced the same result.

4.1.2 Selection of mesh, after a convergence analysis of the results

The part of the algorithm written to generate the mesh in *Ansys* environment (FEM routine) processes the input data on the microscopic geometry, allowing the construction of volumes and surfaces of RVE. At this point, the algorithm requires the definition of elements for the finite element discretization. We selected “20 nodes” solid elements well suited to model curved boundaries and “mesh-only” elements used, in this case, to drive the volume-meshing in a 3-D space (Cricià et al., 2012; Naddeo et al., 2014). The convergence analysis of the results (in terms of mechanical properties) was performed using the variation of the average size of the model mesh (defined as $M=R/i$, being R the radius of the spherical pores) starting by $i = 2$ up to a value at which the percentage error of the FEM model from $i = n$ to $i = n+1$ can be considered negligible for the

purposes of the present work, since a stable asymptotic solution is reached. Stabilization of the result at $i = 15$ was observed, beyond which the error assumed an oscillating low value. For these reasons, an average size of the model mesh equal to $M=R/15$ was chosen with a corresponding percentage error of 0.085. Choosing this value as the average size for the model mesh, the obtained Young modulus was equal to 6.88 % of the Young modulus introduced as input. Therefore, considering E_{ex} the experimentally measured Young modulus of PLLA gel without fillers (i.e., HA), the nanoporous structure model should behave as a continuum characterized by a Young modulus equal to $E_n = E_{ex}/0.069$. It means that the model of the nanoporous structure characterized by an input Young modulus equal to that of the compact and untreated PLLA (E_I) should give, as output, a value equal to E_n . This output value will be the first target for the realization of the nanoporous structure model (nanofiber network).

4.2 Modeling the nanofiber network

Starting from the experimental data, it is possible to calculate the nanoscale porosity through the following relationship:

$$P_n = \frac{P_{tot} - P_M}{1 - P_M} \quad (5)$$

being P_n the nanoscale porosity, P_M the measured micrometric porosity and P_{tot} the experimentally measured global porosity.

Aerogels can exhibit a great structural variety, from branched to compact clusters, depending on the intrinsic or extrinsic conditions (solvent, water content, pH, catalysts, reaction time, etc.). Attempts to model the microstructure of aerogels used Void Expansion Methods (VEM) (Schenker et al., 2009), diffusion-limited aggregation (DLA) (Ma et al., 2001) and Gaussian random field methods (GRF) (Quintanilla et al., 2003). At present, there is no consensus on which simulation strategy is the most adequate. For instance, it is not possible to tune the porosity of the material with standard DLA or GRF. Moreover, some authors argued that the fractal scaling produced by DLA

cannot be observed experimentally. On the other hand, GRF and VEM do not seem to model the physics of gel formation adequately (Morales et al., 2014). In the past, the deviation of aerogels from the prediction for foams has been attributed to the abundance of “dead-ends” (Ma et al., 2002) that are clusters connected to the backbone of the aerogel network at only one point. Other authors (Ma et al., 2000) used the diffusion limited cluster-cluster aggregation (DLCA) algorithm (Gilmore and Katz, 1982) to generate 3D on-lattice aerogel models and the simulations showed that “loop” structure could be important to account for the stiffness of the aerogel (Ma et al., 2001). On the other hand, the DLCA model contains excessive dead ends which lead to an underestimation of the gel modulus at a given density.

Using the commercial image analysis software *Photoshop*, and applying a threshold value, SEM micrographs of the gel were converted into black and white images. Then, the morphological parameters of the aerogel were evaluated. The fibers were substantially arranged in a random network, in all the PLLA aerogel samples without apparent dead ends. No evident clusters or aggregates were found in the fiber network.

Since a great part of the stiffness of an aerogel depends on how the fiber network is connected in the space (Ma et al., 2001), in a first approximation, we imagined a space frame of cylinder-shaped fibers to simulate a structure that basically behaves like an isotropic material. We realized a space frame entirely formed by tetrahedral structures; the idea is to use a modified finite element discretization algorithm to realize the geometric space frame.

4.2.1 RVE identification of the nanometric level

The RVE was chosen as cubic-shaped and discretized in tetrahedra to allow an easily boundary conditions definition; its dimensions were chosen taking care of the statistical intrinsic characteristics, trying to obtain an acceptable degree of isotropy (Cricì et al., 2012). For this reason, we modified a finite element discretization algorithm of *Ansys* to transform the tetrahedral mesh of an unit size cubic RVE into a parametric geometric space frame whose beams match the

tetrahedra edges; subsequently, after deleting the tetrahedral solid mesh, it realizes the mesh of this geometric space frame using linear two-node beam elements in 3-D.

A FEM routine creates identical surface mesh between opposite edges to apply opportune displacement equations that couple homologous nodes on opposite sides depending on the imposed average strain, indicated in the periodic boundary conditions (Ching et al., 2009; Cricrì et al., 2012; Naddeo et al., 2014). In Figure 6, a mesh example is presented. For graphical purposes, less mesh wires than those used in the calculation are represented.

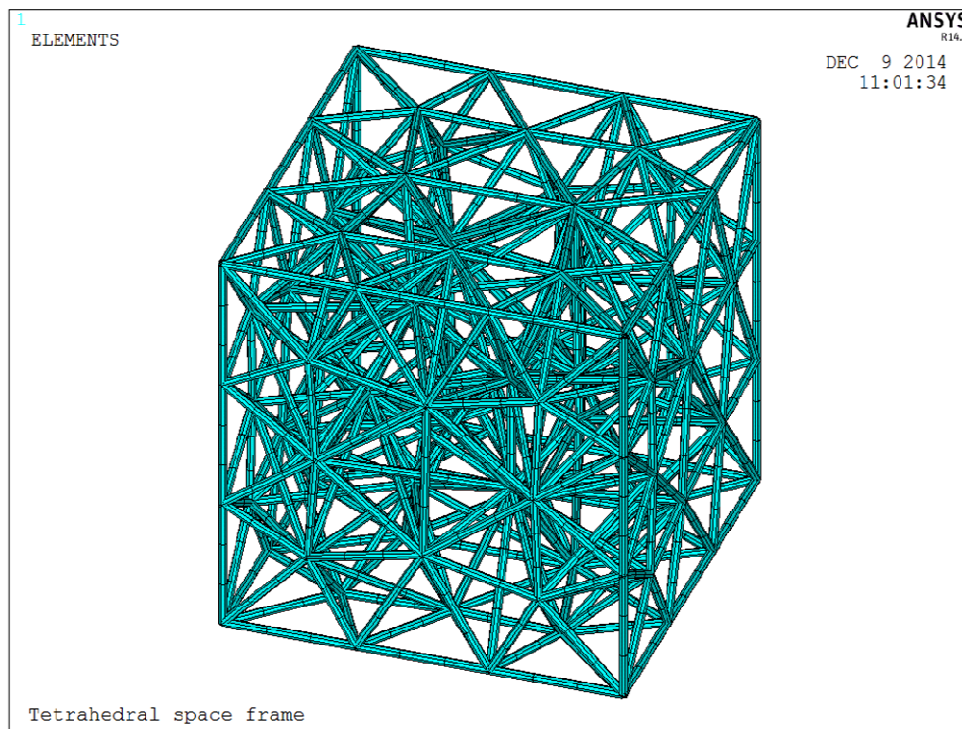


Figure 6: RVE showing a meshed tetrahedral space frame.

4.2.2 Homogenized modules

After the application of the boundary conditions, three static tensile tests and three static shear tests (with imposed average deformations) were performed obtaining all the stiffness matrix components of RVE. Imposing the overall deformation $\langle \varepsilon \rangle = [0, \dots, \langle \varepsilon_i \rangle, \dots, 0]$ and assuming small strains and elastic behavior of the material, for each i-th imposed deformation, the algorithm

calculated all the components of the corresponding i -th column of the stiffness matrix, using the following formulation: from the elastic overall constitutive law, we can write:

$$\overline{\overline{C}}_{hi} = \frac{\langle \sigma_h \rangle}{\langle \varepsilon_i \rangle} \quad \forall h, i = 1, \dots, 6 \quad (6)$$

in which the stress component $\langle \sigma_h \rangle$ is calculated in FEM routine, using the following relationship:

$$\langle \sigma_h \rangle = \frac{\sum_{elem} \sigma_{h \ elem} vol_{elem}}{vol_{RVE}} \quad (7)$$

in which $\sigma_{h \ elem}$ is the h -th stress component of the single element, due to the i -th imposed deformation. In this way, with a single FEM run, characterized by six sequential imposed deformations, the algorithm allowed to calculate all the components of the stiffness matrix with eq. 6 (which provides $\overline{\overline{C}}_{ij}$ values). The algorithm was, finally, able to provide the stiffness and compliance matrices of the examined composite material.

4.2.3 Choice on the RVE size

An original criterion was used (Naddeo et al., 2014) to optimize the size of the RVE, taking into account the accuracy of the statistical computation and the computational burden, assuring that RVE was statistically representative. The assumption was to consider an isotropic behavior for the nanoscale structure. In small RVEs, the position of the fibers may affect the isotropic degree; for this reason, a criterion, directly related to the number of polymeric fibers (number of tetrahedra), was used choosing the size of the RVE. The criterion is based on the minimization of the following function:

$$|\Delta|^2 = \sum_{i,j=1}^6 (C_{i,j} - C_{i,j}^I(\lambda, G))^2 \quad (8)$$

in which C_{ij} is the i, j-th component of the stiffness matrix, extrapolated from FEM calculation, C^I_{ij} is the i, j-th component of the unknown isotropic stiffness matrix, λ and G represent the independent parameters that define the isotropic stiffness matrix (Lamè constants).

The minimization of eq. 8 led to the determination of λ and G , parameters that define the isotropic material closer (with regard to the mechanical behavior) to the material simulated by the *Ansys* calculation. Consequently, the algorithm calculated the parameter δ , given by the ratio between the norm of the “*difference tensor*” $\Delta = C - C^I$ and the norm of the tensor C^I , which provided information about the isotropicity in the model, depending on the size of the RVE (in terms of tetrahedron mean size). Being L_{rve} the edge of the cubic RVE, this criterion showed that, for RVE having tetrahedron mean size smaller than $L_{rve}/12$, the value of the parameter δ tends to a small constant value.

4.2.4 Analysis of the results and verification of the stiffness of the proposed structure

Once realized the RVE space frame, setting the nanoscale porosity P_n , the ratio between the average diameter and the length of the cylindrical fibers was univocally determined. As previously stated, the model of the porous nanoscale structure, characterized by input Young modulus of the compact and untreated PLLA (E_I), should give us as output, a value equal to E_n .

In this case $E_I = 1974 \times 10^3$ kPa (Lu et al., 2007), the experimentally measured Young modulus of PLLA gelled without fillers (HA) (total porosity $P_{tot} = 0.96$) was $E_{ex} = 81$ kPa and the Young modulus as output of the nanoscale structure should be $E_n = E_{ex}/0.0688 = 1177.33$ kPa. FEM model, instead, gave approximately a value of $E_n = 68281$ kPa. Therefore, despite a significant decrease of the structural characteristics (about 96.5 %), the modelled structure remains remarkably rigid and modeling results are very far from the experimental data.

In our opinion, what can determine the further decrease of the mechanical characteristics of the structure, is the particular shape of the cylindrical fibers observed in SEM images (Figures 1 and 2a). They show an average curvature that leads to a buckling tendency, determining a higher

compliance of the entire structure. This observation is supported by a previous study (Ma et al., 2002) revealing that loop structure is lacking in the modeled gels. For this reason, a further modeling was developed to address loop formation, during the gel aggregation process, discovering that bending was the major mode of deformation of the network. Also other authors (Pirard and Pirard, 1997) proposed a mechanism based on the preferential buckling of the network around larger pores.

To take into account these characteristics, first, we realized a parametric modeling of a single cylindrical curved fiber, that was modeled choosing, as the cylinder axis, a spline curve interpolating three points, two of which coincident with the endpoints of the rod of length L and a third in a central position at a distance d from the rod axis. We computed the Young modulus of the curved rod varying the curvature determined by the size of the parameter d , maintaining volume and section at a constant value and considering the force directed along the line connecting the two end points of the curved rod. As a result, we obtained a decrease of the Young modulus of more than two orders of magnitude in the transition from $d = 0$ to $d = 0.5L$. For this reason, we implemented, in the main algorithm, a routine that substitutes the beams of the Space with parametric curved rods. FEM discretization was realized using quadratic (three-node) multi-layered pipe elements in 3-D, suitable to model the filler (HA) that tends to cover PLLA fibers. A convergence analysis of the results was made, taking into account the computational effort.

4.2.5 Identification of the configuration that achieves the desired results in terms of the mechanical response

The total volume of the described structure is:

$$V_p = \sum_{i=1}^n L_i(d)\Sigma \quad (9)$$

being n the total number of fibers, V_p the volume occupied by the polymeric matrix, L_i the length of the i -th spline, which is a function of the parameter d , and Σ the section of the fiber that

does not vary with i . The introduced routine produced an interpolating spline curve of output data points that describes the function $E = E(d)$ maintaining constant $P_n = 0.8$ using the relationship (9). Introducing $E = 1177.33$ kPa, the interpolating curve gives the value $d = 0.4514$. Therefore, introducing this value as input, it is possible to reach a value equal to about $E_n = 1178$ kPa; i.e., very close to that expected. Introducing this value as input in the micrometric porosity model previously described, we obtained a value of $E_{FEM} = 81.41$ kPa, that is very close to the one experimentally measured: $E_{ex} = 81$ kPa.

4.3 Modeling of the filler (HA)

The modeling of HA filler was obtained starting from information coming from SEM images and studying the mechanical experimental curves. In particular, it was possible to make some considerations on the trend of the experimental curve of Young modulus when the weight percentage of the filler was increased (Table 1). SEM images show that multi-layer decoration of the nanofibers increases with the weight percentage of HA up to 30 % w/w (Figure 1b). For higher HA percentages, Young modulus only slightly increases. We supposed that this is an indication of the fact that exceeding HA tended to deposit inside the micrometric pores of the structure, as shown in Figure 2c. It is, therefore, possible to imagine that two coaxial cylinders are formed, in which the external one is the filler that realizes a sort of multi-layer coating or decoration on the polymer matrix, represented by the inner cylinder. SEM images (Figure 2b) indicate an extensive HA nanoparticles coverage of the nanofibers in the case of a relatively open network; this coverage is not homogeneous in thickness and spot decorations are evident. We have no indication about the coverage of the nanofibers located in the most internal part of the network. If HA adhesion is due to electrostatic interactions among HA nanoparticles and PLLA nanofibers, multi-layer decoration can be explained as nanoparticles adhesion until the local surface electric charge has been completely neutralized. Moreover, since electrostatic charges tend to dispose on the external surfaces of a solid system, it is possible that nanofibers in the internal part of the network could bear a reduced or zero

electric charge and, as a consequence, are not (or partly) covered by HA nanoparticles. For these reasons, we decided to model the second cylinder as partially covering the inner one, introducing a “loaded surface index” defined as $C_i = L_c/L$, being L_c the portion of PLLA cylinder fiber covered by HA and L the length of the cylinder fiber. The idea is to model the generic PLLA fiber coated by HA as shown in Figure 7.

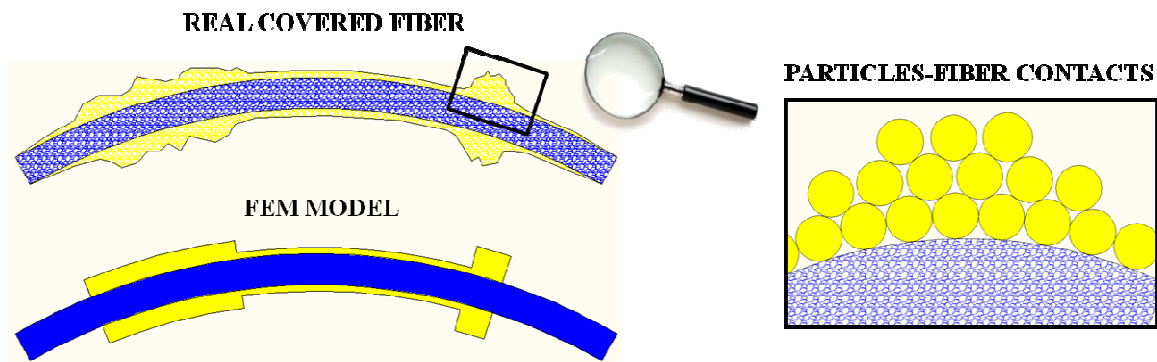


Figure 7: Schematic example of a covered fiber section: on the left, relation between real fiber and FEM model; on the right, a detail of the contact between HA particles and PLLA fiber.

For this reason, it was first realized a finite element model of a single partially covered rod ($C_i = 0.33$). FEM tensile tests confirmed the plateau effect of the Young modulus with the increasing weight percentage of HA recorded in the experimental tests (Figure 8) for HA weight percentages larger than 30 % w/w.

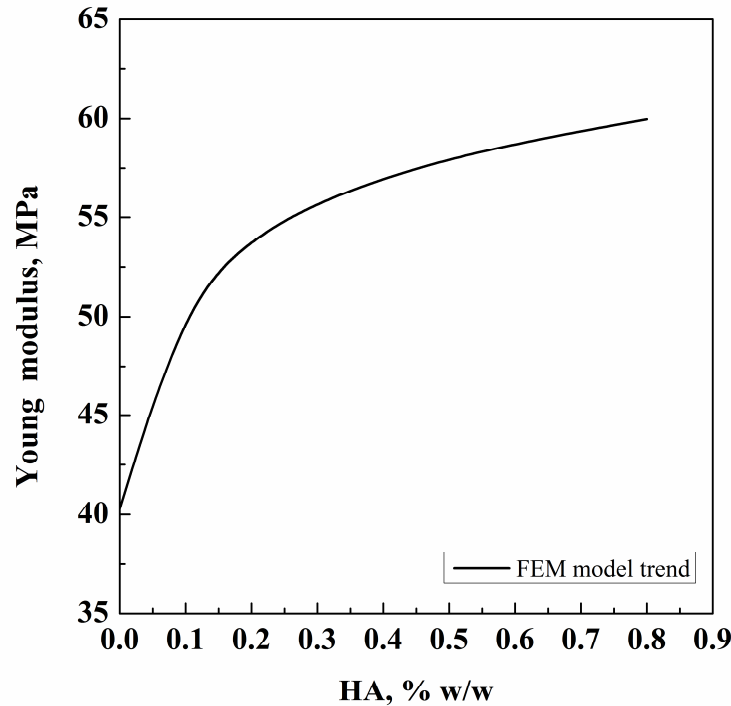


Figure 8: Plateau effect of the Young modulus with the increasing weight percentage of HA for a single fiber FEM model.

The next step was the implementation of an additional routine able to:

- a) select a given percentage of geometric lines (forming the axis of symmetry of the curved cylindrical fibers) according to a given “loaded surface index” C_i (defined as above);
- b) calculate the thickness of HA coating based on the weight percentage of HA and the specific weight of both PLLA and HA;
- c) mesh the selected lines, representing the areas covered by HA, with multi-layered elements described in the previous paragraph.

In Figure 9, a cubic RVE of the nanostructured model, in which it is possible to distinguish the inflected PLLA fibers partially covered by HA, is shown.

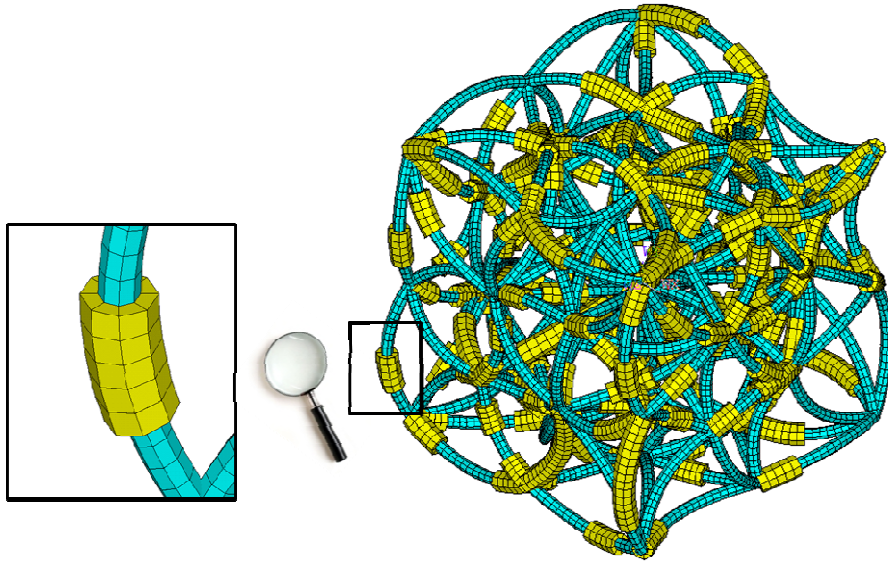


Figure 9: Explanatory example of a cubic RVE of the nanostructured model: PLLA (blue elements); HA (yellow elements).

We calibrated the “loaded surface index” starting from $C_i = 0.0$ to approximate the resulting Young modulus to the corresponding experiments, with the maximum weight percentage of HA. Introducing for HA as input, a Young modulus equal to $E_{HA} = 114$ GPa (Gilmore and Katz, 1982; Katz and Ukraincik, 1971) and a Poisson ratio equal to $\nu_{HA} = 0.262$ (Ching et al., 2009), we obtained for the model a Young modulus equal to $E = 122.82$ kPa in correspondence of $C_i = 0.14$, which is a value fairly close to the one experimentally obtained ($E_{ex} = 122$ kPa). The resulting value for the “loaded surface index” can be easily explained also taking into account the quasi-spherical shape of HA particles; the contact on the nanofibers, therefore, occurs only on the small areas of contact between PLLA fiber and the quasi-spherical shaped HA particles, leaving the remaining parts free from interactions (see also Figure 7).

Once the “loaded surface index” was set at $C_i = 0.14$, we realized a series of finite element analyses to model all the other weight percentages of HA experimentally used, assuming that the “loaded surface index” remained constant. The curve in Figure 10 shows the comparison of experimental and numerical results in terms of Young modulus.

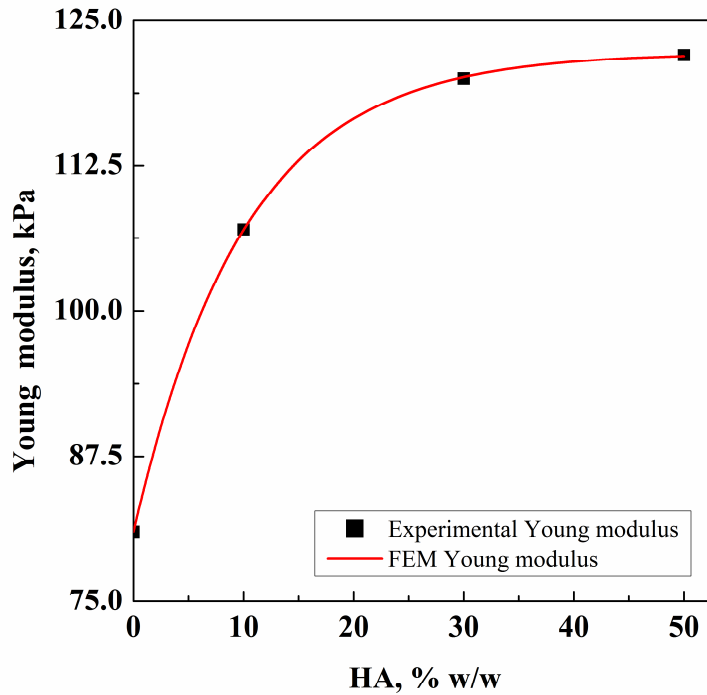


Figure 10: Superposition of the numerical results on the experimental results.

It is useful to remind that FEM results were obtained by the combination of both FEM model of the composite micrometric porous structure and FEM model of the nanoscale structure, varying only the weight percentage of HA introduced in input in FEM modeling algorithm. This comparison also confirms the plateau effect experimentally recorded for HA loadings larger than 30 % w/w.

5 Discussion, conclusions and perspectives

Summarizing the results, the combination of a FEM model of the composite micrometric porous structure, based on the theory of hcp, and of the nanoscale structure modeled as a quite regular space frame of isotropic curved fibers, without any “dead-ends” or discontinuities, is able to well reproduce our experimental results on PLLA scaffolds, when we set a porosity equal to the one experimentally recorded both at micrometric and at nanometric level. A mechanical response very close to the experimental one was obtained. It confirms the hypothesis, corroborated by other works in the literature (Ma et al., 2002; Pirard and Pirard, 1997), that the decrease of the mechanical

properties of aerogels depends on how the fiber network is connected in the space and that bending is the major mode of deformation of the network. Furthermore, the parametric modeling of HA nanoparticles, forming a sort of cylinder that cover PLLA fibers with a limit in “loaded surface” at higher HA amounts, confirms the reinforcement mechanism as the tendency of HA to increase the fiber thickness of the already covered zones. Therefore, HA coverage of PLLA fibers increases their stiffness and produces the macroscopic increase of Young modulus. This phenomenon ends when electrostatic force between external HA particles and PLLA fibers becomes negligible. As a consequence, exceeding HA nanoparticles start to deposit on the bottom of the microporous cavities located in the scaffold and do not give any further substantial contribution to the mechanical resistance of the structure. It is possible to formulate another hypothesis about the overall stiffness of the nanofibrous structure beyond the range of small displacements: HA nanoparticles decoration obstacles nanofibers relative motion, increasing the friction and partly blocking them. It is also possible that rigidity increases and movement obstacle mechanisms can coexist.

In the perspective, the idea is to use this model as a tool to understand/confirm the interactions among other structures (pores/nanofilaments) and/or materials involved or to predict how optimized structures can be obtained.

Numerical analysis can allow to discover the parameters to be controlled during the supercritical process. An example might be the analysis of the influence, on the mechanical behavior of the structure, of the porosity imparted by the porogen, that can be directly related also to the pressure used to produce the contact among the porogen particles that induces the interconnections among the pores.

Possible future developments of FEM model may be: the development of a method to estimate the amount of precipitated particles for a better approximation of the real composite structure; the evaluation of the effect of large deformations, implementing new material characteristics to cover the field of geometrical and material nonlinearity and the introduction of the influence of the mutual contacts among the various composite components.

References

- Baldino, L., Cardea, S., De Marco, I., Reverchon, E., 2014a. Chitosan scaffolds formation by a supercritical freeze extraction process. *The Journal of Supercritical Fluids* 90, 27-34.
- Baldino, L., Cardea, S., Reverchon, E., 2014b. Supercritical assisted enzymatic membranes preparation, for active packaging applications. *Journal of Membrane Science* 453, 409-418.
- Brunner, G., 2010. Applications of supercritical fluids. *Annual review of chemical and biomolecular engineering* 1, 321-342.
- Cardea, S., Baldino, L., Scognamiglio, M., Reverchon, E., 2014. 3D PLLA/Ibuprofen composite scaffolds obtained by a supercritical fluids assisted process. *Journal of Materials Science: Materials in Medicine* 25, 989-998.
- Cardea, S., Gugliuzza, A., Rappo, E.S., Aceto, M., Drioli, E., Reverchon, E., 2006. Generation of PEEK-WC membranes by supercritical fluids. *Desalination* 200, 58-60.
- Cardea, S., Reverchon, E., 2011. Nanostructured PVDF-HFP membranes loaded with catalyst obtained by supercritical CO₂ assisted techniques. *Chemical Engineering and Processing: Process Intensification* 50, 630-636.
- Ching, W., Rulis, P., Misra, A., 2009. Ab initio elastic properties and tensile strength of crystalline hydroxyapatite. *Acta Biomaterialia* 5, 3067-3075.
- Costantino, P.D., Friedman, C.D., 1994. Synthetic bone graft substitutes. *Otolaryngologic Clinics of North America* 27, 1037-1074.
- Cricri, G., Garofalo, E., Naddeo, F., Incarnato, L., 2012. Stiffness constants prediction of nanocomposites using a periodic 3D-FEM model. *Journal of Polymer Science Part B: Polymer Physics* 50, 207-220.
- Duarte, A.R.C., Mano, J.F., Reis, R.L., 2009. Preparation of starch-based scaffolds for tissue engineering by supercritical immersion precipitation. *The Journal of Supercritical Fluids* 49, 279-285.
- Flautre, B., Descamps, M., Delecourt, C., Blary, M., Hardouin, P., 2001. Porous HA ceramic for bone replacement: role of the pores and interconnections—experimental study in the rabbit. *Journal of Materials Science: Materials in Medicine* 12, 679-682.
- Gilmore, R., Katz, J., 1982. Elastic properties of apatites. *Journal of Materials Science* 17, 1131-1141.
- Goldberg, V.M., 1992. Natural history of autografts and allografts, *Bone implant grafting*. Springer, pp. 9-12.
- Harris, L.D., Kim, B.-S., Mooney, D.J., 1998. Open pore biodegradable matrices formed with gas foaming.
- Hu, Z., Notarberardino, B., Baker, M., Tabor, G., Hao, L., Turner, I., Yang, L., 2009. On Modeling Bio-Scaffolds: Structural and Fluid Transport Characterization Based on 3-D Imaging Data. *Tsinghua Science & Technology* 14, 20-23.
- Jungreuthmayer, C., Jaasma, M.J., Al-Munajjed, A.A., Zanghellini, J., Kelly, D.J., O'Brien, F.J., 2009. Deformation simulation of cells seeded on a collagen-GAG scaffold in a flow perfusion bioreactor using a sequential 3D CFD-elastostatics model. *Medical engineering & physics* 31, 420-427.
- Kapfer, S.C., Hyde, S.T., Mecke, K., Arns, C.H., Schröder-Turk, G.E., 2011. Minimal surface scaffold designs for tissue engineering. *Biomaterials* 32, 6875-6882.
- Katz, J., Ukraincik, K., 1971. On the anisotropic elastic properties of hydroxyapatite. *Journal of biomechanics* 4, 221-227.
- LeGeros, R.Z., 2002. Properties of osteoconductive biomaterials: calcium phosphates. *Clinical orthopaedics and related research* 395, 81-98.
- Levit, N., Tepper, G., 2004. Supercritical CO₂-assisted electrospinning. *The Journal of Supercritical Fluids* 31, 329-333.

- Li, S.H., De Wijn, J.R., Layrolle, P., De Groot, K., 2002. Synthesis of macroporous hydroxyapatite scaffolds for bone tissue engineering. *Journal of biomedical materials research* 61, 109-120.
- Liu, J., Shen, Z., Lee, S.-H., Marquez, M., McHugh, M.A., 2010. Electrospinning in compressed carbon dioxide: Hollow or open-cell fiber formation with a single nozzle configuration. *The Journal of Supercritical Fluids* 53, 142-150.
- Lu, J., Qiu, Z., Yang, W., 2007. Fully biodegradable blends of poly (l-lactide) and poly (ethylene succinate): miscibility, crystallization, and mechanical properties. *Polymer* 48, 4196-4204.
- Ma, H.-S., Prévost, J.-H., Jullien, R., Scherer, G.W., 2001. Computer simulation of mechanical structure–property relationship of aerogels. *Journal of non-crystalline solids* 285, 216-221.
- Ma, H.-S., Prévost, J.-H., Scherer, G.W., 2002. Elasticity of DLCA model gels with loops. *International journal of solids and structures* 39, 4605-4614.
- Ma, H.-S., Roberts, A.P., Prévost, J.-H., Jullien, R., Scherer, G.W., 2000. Mechanical structure–property relationship of aerogels. *Journal of non-crystalline solids* 277, 127-141.
- Ma, P.X., 2004. Scaffolds for tissue fabrication. *Materials today* 7, 30-40.
- Ma, P.X., Zhang, R., 1999. Synthetic nano-scale fibrous extracellular matrix.
- Malafaya, P., Silva, G., Baran, E., Reis, R., 2002a. Drug delivery therapies I: general trends and its importance on bone tissue engineering applications. *Current Opinion in Solid State and Materials Science* 6, 283-295.
- Malafaya, P., Silva, G., Baran, E., Reis, R., 2002b. Drug delivery therapies II.: strategies for delivering bone regenerating factors. *Current Opinion in Solid State and Materials Science* 6, 297-312.
- Milan, J.-L., Planell, J.A., Lacroix, D., 2009. Computational modelling of the mechanical environment of osteogenesis within a polylactic acid–calcium phosphate glass scaffold. *Biomaterials* 30, 4219-4226.
- Mooney, D.J., Baldwin, D.F., Suh, N.P., Vacanti, J.P., Langer, R., 1996. Novel approach to fabricate porous sponges of poly (D, L-lactic-co-glycolic acid) without the use of organic solvents. *Biomaterials* 17, 1417-1422.
- Morales, R., da Cunha, C., Rambo, C., 2014. A complex network approach for the growth of aerogels. *Physica A: Statistical Mechanics and its Applications* 406, 131-138.
- Naddeo, F., Cappetti, N., Naddeo, A., 2014. Automatic versatile parametric procedure for a complete FEM structural analysis of composites having cylinder-shaped reinforcing fibres. *Computational Materials Science* 81, 239-245.
- Olivares, A.L., Marsal, È., Planell, J.A., Lacroix, D., 2009. Finite element study of scaffold architecture design and culture conditions for tissue engineering. *Biomaterials* 30, 6142-6149.
- Pirard, R., Pirard, J.-P., 1997. Aerogel compression theoretical analysis. *Journal of non-crystalline solids* 212, 262-267.
- Pisanti, P., Yeatts, A.B., Cardea, S., Fisher, J.P., Reverchon, E., 2012. Tubular perfusion system culture of human mesenchymal stem cells on poly-L-lactic acid scaffolds produced using a supercritical carbon dioxide-assisted process. *Journal of Biomedical Materials Research Part A* 100, 2563-2572.
- Prosapio, V., Reverchon, E., De Marco, I., 2014. Antisolvent micronization of BSA using supercritical mixtures carbon dioxide+ organic solvent. *The Journal of Supercritical Fluids* 94, 189-197.
- Quintanilla, J., Reidy, R., Gorman, B., Mueller, D., 2003. Gaussian random field models of aerogels. *Journal of applied physics* 93, 4584-4589.
- Rainer, A., Giannitelli, S.M., Accoto, D., De Porcellinis, S., Guglielmelli, E., Trombetta, M., 2012. Load-adaptive scaffold architecturing: a bioinspired approach to the design of porous additively manufactured scaffolds with optimized mechanical properties. *Annals of biomedical engineering* 40, 966-975.
- Rajagopalan, S., Robb, R.A., 2006. Schwarz meets Schwann: design and fabrication of biomorphic and durataxic tissue engineering scaffolds. *Medical image analysis* 10, 693-712.

Reverchon, E., Adami, R., 2013. Supercritical assisted atomization to produce nanostructured chitosan-hydroxyapatite microparticles for biomedical application. *Powder Technology* 246, 441-447.

Reverchon, E., Baldino, L., Cardea, S., De Marco, I., 2012. Biodegradable synthetic scaffolds for tendon regeneration. *Muscles, Ligaments and Tendons Journal* 2, 181.

Reverchon, E., Cardea, S., 2005. Formation of polysulfone membranes by supercritical CO₂. *The Journal of Supercritical Fluids* 35, 140-146.

Reverchon, E., Cardea, S., 2012. Supercritical fluids in 3-D tissue engineering. *The Journal of Supercritical Fluids* 69, 97-107.

Reverchon, E., Cardea, S., Rapuano, C., 2008. A new supercritical fluid-based process to produce scaffolds for tissue replacement. *The Journal of Supercritical Fluids* 45, 365-373.

Reverchon, E., Osseo, L.S., Gorgoglione, D., 1994. Supercritical CO₂ extraction of basil oil: characterization of products and process modeling. *The Journal of Supercritical Fluids* 7, 185-190.

Reverchon, E., Pisanti, P., Cardea, S., 2009. Nanostructured PLLA– Hydroxyapatite Scaffolds Produced by a Supercritical Assisted Technique. *Industrial & Engineering Chemistry Research* 48, 5310-5316.

Sandino, C., Planell, J., Lacroix, D., 2008. A finite element study of mechanical stimuli in scaffolds for bone tissue engineering. *Journal of biomechanics* 41, 1005-1014.

Schenker, I., Filser, F.T., Herrmann, H.J., Gauckler, L.J., 2009. Generation of porous particle structures using the void expansion method. *Granular Matter* 11, 201-208.

Stamatialis, D.F., Papenburg, B.J., Gironés, M., Saiful, S., Bettahalli, S.N., Schmitmeier, S., Wessling, M., 2008. Medical applications of membranes: drug delivery, artificial organs and tissue engineering. *Journal of Membrane Science* 308, 1-34.

Subra, P., Vega-Bancel, A., Reverchon, E., 1998. Breakthrough curves and adsorption isotherms of terpene mixtures in supercritical carbon dioxide. *The Journal of Supercritical Fluids* 12, 43-57.

Visscher, G., Robison, R., Maulding, H., Fong, J., Pearson, J., Argentieri, G., 1985. Biodegradation of and tissue reaction to 50: 50 poly (DL-lactide-co-glycolide) microcapsules. *Journal of biomedical materials research* 19, 349-365.

Zhang, R., Ma, P.X., 1999a. Poly (α -hydroxyl acids)/hydroxyapatite porous composites for bone-tissue engineering. I. Preparation and morphology.

Zhang, R., Ma, P.X., 1999b. Porous poly (L-lactic acid)/apatite composites created by biomimetic process.